Open Access

Journal of Energy and Power Technology

LIDSEN Publishing Inc.

Original Research

Non-Isothermal Compressible Flow Model for Analyzing the Effect of High CO_2 Inlet Flow Rate on Particle Size in a Supercritical Antisolvent Process

Regiani Aparecida de Almeida [1, *], Ricardo Vicente de Paula Rezende [1], Flavia Aparecida Reitz Cardoso [2], Lucio Cardozo Filho [1]

1. Department of Chemical Engineering, Universidade Estadual de Maringá, 87020-900, Maringá-PR, Brazil; E-Mails: regy.al@gmail.com; rezendervp@gmail.com; lucio.cardozo@gmail.com
2. Department of Mathematics, Universidade Federal Tecnológica do Paraná, 87301-005, Campo Mourão-PR, Brazil; E-Mail: flaviareitz@gmail.com

* **Correspondence:** Regiani Aparecida de Almeida; E-Mail: regy.al@gmail.com

Academic Editor: Faik Hamad

Special Issue: Multi-phase Flow with and without Heat Transfer

Journal of Energy and Power Technology
2023, volume 5, issue 2
doi:10.21926/jept.2302016

Received: December 17, 2022
Accepted: April 05, 2023
Published: April 18, 2023

Abstract

In this work with CFD simulations, the evaluation of the supercritical anti-solvent (SAS) process for producing nanoparticles from an expanded solution of ethanol/solute in carbon dioxide is reported. The influence of the solution and antisolvent flow rates on mean particle size, the flow dynamic, and the supercritical mixture's jet velocity must be well established in the literature and analyzed. The high flow rate of the anti-solvent resulted in increased mean particle sizes for all studied cases. At the lowest flow rate of CO_2 examined, an increase in the solvent flow rate [0.3-1.0] ml/min initially led to a decrease of 11.2% in the mean particle diameter (MPD); however, further increasing the solvent flow rate [1.0-2.0]ml/min was an increase of 33% in this parameter. At the highest CO_2 flow rate, the behavior of MPS was the opposite; it had a rise de 13.5% in MPD with an increase in solvent flow rate; further increasing the flow rate of the solvent, there was a drop of 8.6% in MPD. Significant variations in the temperature lead to large fluctuations in the particle diameters. At last, the contact zones

between CO_2 and ethanol were delimited, favoring the understanding of the influence of the flow patterns generated by the variation of the flow rates in the mean particle diameters.

Keywords
Computational fluid dynamics; SAS process; particle size; jet velocity

1. Introduction

Increasingly, nanotechnology appears in applications in the most diverse areas of science. In particular, supercritical CO_2 can be employed in applications in various fields, many new works have been published with such applications in the food, pharmaceutical and cosmetics industries, covering: essential and seed oil extraction, particle formation, impregnation and polymer synthesis [1-3]. Supercritical technology has been used to obtain nanoparticles of various drugs, particle size is a critical parameter affecting precipitated drugs' bioavailability and physical properties.

Computational fluid dynamics (CFD) has contributed to many numerical studies on industrial processes that use supercritical carbon dioxide with an anti-solvent action [4]. High diffusivity and low viscosity of supercritical fluids favor the precipitation of fine, uniform particles. Despite the difficulties in predicting flow variables in turbulent flow, mathematical models assist in interpreting and comprehending experimental results [5]. Also, the processes and improvements of the used equipment can be provided [6-8].

One of the objectives of developing nanoparticles of drugs in a solid state is to increase the solubility of the drug while maintaining its stability. Particle size reduction is increasingly emerging to modify the specifications of solid forms such as solubility, stability, dissolution rate and bioavailability, without changing the desired effect of the product. Despite having the same composition as the corresponding material, nanometer-scale particles exhibit exceptional optical, electrical, thermal, and magnetic characteristics due to side effects. One of them is the ability to bind to other molecules, a fact that makes these materials multifunctional and can be used in much applications current research has been aimed at improving properties such as: shape and size distribution to better suit specific applications [9]. Several processes are employed for the precipitation of particles. Physical techniques include grinding, gas condensation, electrospray, lithography, and thermodecomposition. Some aspects represent disadvantages in using these techniques, such as thermal degradation, long extraction times, solvent residues and loss of volatile compounds, as is the case with the extraction of essential oils [10, 11].

Particularly the SAS process employs CO_2 in a supercritical state, and assumes that organic solvents are completely miscible in the supercritical fluid used as antisolvent [12, 13]; it has some advantages over other techniques such as: it produces a dry and solvent-free product, high conversion coefficient and high reaction rates [14]. Considering the phase behavior involving the ternary system, solute-solvent and supercritical fluid, the interaction between this mixture that happens with the dispersion of the solution inside the precipitation chamber charged with CO_2 is fundamental to determining good operating conditions [15], also in this sense, several works involving the optimization of process parameters covering the extraction efficiency have been published [10, 16]. Specifically the values of the flow rate of CO_2 and the flow rate of solution (solute

and organic solvent) are directly linked to the success of the supercritical extraction process. To adjust these variables experimentally to obtain optimal particle sizes, occur difficulties such as a large number of experiments, which increases the time and cost in the laboratory to obtain a final quality product. In addition to the flow rates mentioned above, other process variables must be combined to obtain an excellent precipitated final product. They are operating temperature and pressure, initial solute concentration, precipitation chamber geometry, injection capillary geometry, and physical-chemical properties of the chemical species to be precipitated. Such parameters also directly impact the particle sizes obtained [13, 17-20].

As for the mathematical modeling of the flow in the SAS process, the physical nature of flows in supercritical expansion involves more than one phase, the presence of very small particles, is compressible, turbulent, not isothermal, thus involves numerical and mathematical difficulties inherent in multiphase flow [6]. Some simplifications have been proposed: modeling in a single phase, stationary regime, and compressible and non-isothermal flow has been employed by some authors [21, 22]. Still, others consider incompressible and isothermal flow with significant results [23]. Even so, numerical studies presented in this work are pretty scarce in the literature. They can accurately predict the impacts of the described variables on the flow behavior and, consequently, on the particle sizes obtained [13, 24].

Experimental and numerical studies indicate the importance of CO_2 and solute-solvent mixture flow rates for process efficiency [25, 26]; in particular, from a numerical point of view, when high flow rates are considered in the boundary conditions it causes numerical instabilities, making convergence a challenge. Another numerical challenge that also characterizes a gap in the literature concerns the compressible and non-isothermal nature of the flow in supercritical state flow. Studies about the impact of the compressibility of the flow in the SAS process and flow rates on mean particle size over a wide range of temperatures and pressure were not yet reported in the literature. The SAS method's heat transfer during the particle formation also greatly influences the particle size obtained. However, it is still very little studied using CFD tools [27].

At a temperature of 318 K and a pressure range of 10 to 24 MPa, [28] determined experimentally that an increase in the CO_2 flow rate decreases the particle size distribution. [25] successfully carried out the micronization of minocycline hydrochloride to develop a three-dimensional model for the flow dynamics of the process. A turbulence and supersaturation model that could evaluate the performance of the micronization cell and its adjustability to a supercritical carbon dioxide/ethanol/solute ternary system at constant temperature and pressure was proposed, and analysis of the effects of solute concentration and CO_2/ethanol flow rates on the particle size distribution permitted to understand that the SAS micronization of minocycline is a very fast and it takes place in the solution jet or its close vicinity. The model was validated by simulating the dispersion of methylene chloride in carbon dioxide in the system described by [29]. Other results of this study showed that the solution flow rate minimally affects the average size of the particles. However, its increase contributes to a narrow size distribution range and an increased homogeneity of the precipitated particles.

[30] conducted another study on the same chemical species system analyzed by [25]. The researchers highlighted that an increase in the injection velocity and solute solution concentration results in the precipitation of smaller particles with more regular formats. However, this is not a general rule; the shape of the obtained solids and their average sizes depend on several parameters

such as *T*, *p*, inlet flow rates, chamber and capillary injection geometries, and the physicochemical nature of the solutes.

More recently, [20] used the population balance equation to study the effect of operational parameters of the SAS process on the particle size of co-crystal-pure powders of naproxen-nicotinamide obtained at *T* = 310 K and *p* = 100 bar. At solution inlet flow rate of 6.0 to 13.0 ml/min and CO_2 inlet flow rate of 10.0 to 81.9 ml/min, it was observed that solution and CO_2 flow rates do not significantly affect co-crystal precipitation and particle size distribution. However, the results showed that a more prosperous solvent environment provides better conditions for crystallization.

Some approaches have been reported in the literature regarding the mathematical modeling of the particle precipitation process. In contrast to previous authors, an elaborate model was proposed by [8] for the micronization of beta carotene using dichloromethane as a solvent and supercritical carbon dioxide as an anti-solvent. In addition to the hydrodynamic processes of the jet, the proposed model involves mass balance, kinetic energy, and dissipation rate (standard *k*-*ε* turbulence model) in an isothermal regime and an expression for particle growth.

Such as the work presented by [21] for the precipitation of β-carotene in supercritical fluids with a significant variation in the Schmidt number, improved geometry was studied. Momentum, species, mass, and energy balance equations, *k*-*ε* turbulence model, micro-mixture model, and population balance equation were employed to provide mathematical formulation capable of describing the observed turbulent mixture phenomena for different dimensions of the capillary nozzles in the SAS process. [31] used a population balance equation to study the mixed-product removal crystallizer. In that work, a range of low CO_2 flow rates was investigated (20-40 ml/min). The numerical methodology was viable to predict particle size and particle size distribution according to the specific necessities of a different system in various operating conditions.

Given the experimental difficulties imposed by the combination of several process parameters previously described to obtain particles of small sizes via the SAS technique no numerical works were found in the literature that takes into account the compressible and non-isothermal characteristics of the supercritical mixture in the SAS process [32]. A numerical study of the SAS precipitation chamber based on computational fluid dynamics, considering the compressibility of the flow described by the Peng-Robinson equation of state (EOS) and its non-isothermal character, is proposed in the present work. The objective is to evaluate the effect of the high flow rate of CO_2 and the temperature variation on jet dispersion and mean particle size. The model was solved by the finite volume method in Ansys Fluent commercial code.

2. Mathematical Modeling

The mathematical model is composed of the Navier-Stokes equations coupled to the *k*-*ω* turbulence model, and a compressible and non-isothermal mixture of fluids was considered from the Peng-Robinson EOS and the energy equation respectively. The population balance equation was also used to describe the mean size of the precipitated particles in the SAS process based on the work of [31]. The effect of solute in the mixture properties was not considered because its concentration in the solution was very low. However, the population balance equation modeled the presence of the solute in this case as a solute concentration in the feed solution.

2.1 Thermodynamic Modeling

The compressibility of the mixture with pressure and temperature is modeled via the density of the mixture in the supercritical state, which was calculated with the Peng-Robinson cubic equation with Van der Waals mixing rule as shown in **Eq.** (1)-(3):

$$p = \frac{RT}{v - b_m} - \frac{a_m(T)}{v(v + b_m) + b_m(v - b_m)}, \tag{1}$$

where

$$a_m(T) = \sum_{\alpha}\sum_{\beta} x_\alpha x_\beta a_{\alpha\beta} \tag{2}$$

and

$$b_m(T) = \sum_{\alpha}\sum_{\beta} x_\alpha x_\beta b_{\alpha\beta}\,, \tag{3}$$

The parameters used for both CO_2 and ethanol systems are: $k_{\alpha\alpha} = l_{\alpha\alpha} = 0, k_{12} = 0.0967$ and $l_{12} = -0.000966$. This formulation makes it possible to study the importance of solving the system resulting from equations in a non-isothermal regime.

2.1.1 Mixture Viscosity

A correlation reported by [17] (**Eq.** (4)) was used to determine the viscosity of the systems:

$$\mu_{\text{mix}} = \exp\left(\varphi_{\text{CO}_2} \ln \mu_{\text{CO}_2} + \varphi_{\text{etanol}} \ln \mu_{\text{etanol}}\right), \tag{4}$$

where $\mu_{\text{CO}_2} = 6.21\times10^{-5}$ and $\mu_{\text{etanol}} = 0.794\times10^{-3}$.

The mathematical model described below represents the compressible turbulent flow of the binary mixture of ethanol and CO_2. The model considers particle precipitation based on population balance.

2.2 Conservation Equations

Conservation equations are expressed for a control volume. The volume is fixed in the three-dimensional space of the computational domain being considered. The *k-ω* turbulence model was used with the mass-weighted average (Favre averaging) technique to separate the turbulent fluctuations of average flow. In accordance, a local variable average is defined as $\tilde{y} = \frac{\overline{\rho y}}{\bar{\rho}}$, where *ρ* is the variable density of the mixture. Thus, the field of any variable *y* may be decomposed as where the superscripts symbols and ~ denote the Reynolds and Favre average numbers, respectively. The conservation equations for average flow are shown below.

2.2.1 Continuity Equation

$$\frac{\partial \bar{\rho}}{\partial t} + \frac{\partial \left(\bar{\rho}\widetilde{u_j}\right)}{\partial x_j} = 0. \tag{5}$$

2.2.2 Momentum Conservation Equation

$$\frac{\partial (\bar{\rho}\tilde{u}_i)}{\partial t} + \frac{\partial \left(\bar{\rho}\tilde{u}_i\tilde{u}_j - \tilde{\tau}_{ij}\right)}{\partial x_j} = \frac{\partial \bar{p}}{\partial x_j}, \tag{6}$$

where is the pressure, and $\tilde{\tau}_{ij}$ is the Reynolds stress tensor.

2.2.3 Energy Equation

$$\frac{\partial \left(\bar{\rho}\tilde{h}_{tot}\right)}{\partial t} + \frac{\partial \left(\bar{\rho}\tilde{h}_{tot}\tilde{u}_j\right)}{\partial x_j} = \frac{\partial}{\partial x_j}\left[\bar{\rho}\left(\frac{k_m + k_T}{c_p}\right)\frac{\partial \widetilde{T}}{\partial x_j}\right] + \frac{1}{c_p}\left[\frac{\partial \bar{p}}{\partial t} + \frac{\partial \left(\tilde{u}_j\bar{p}\right)}{\partial x_j}\right], \tag{7}$$

where *T* is the temperature, $\tilde{h}_{tot}$ is the total enthalpy, k_m is the molecular thermal conductivity, and k_T is the turbulent thermal conductivity, and c_p is the heat capacity at constant pressure.

2.2.4 Species Conservation Equation

$$\frac{\partial (\bar{\rho}\tilde{y}_\alpha)}{\partial t} + \frac{\partial \left(\bar{\rho}\tilde{u}_j\tilde{y}_\alpha\right)}{\partial x_j} = \frac{\partial}{\partial x_j}\left[\bar{\rho}(\Gamma_m + \Gamma_T)\frac{\partial \tilde{y}_\alpha}{\partial x_j}\right], \tag{8}$$

where $\tilde{y}_\alpha$ is the mass fraction of the component α; Γ_T is the turbulent diffusion coefficient, and the molecular diffusion coefficient of ethanol and CO_2 mixture was $\Gamma_m = 1.69\times10^{-8}\mathrm{m}^2/\mathrm{s}$, [25].

2.2.5 Particle Precipitation

The population balance developed by [33] based on McCabe Law was used for precipitation. It considers that particles of the same geometry, but different sizes, grow at the same growth rate. Thus, after the hypothesis made for the general population balance equation, according to [31], it was considered:

$$\frac{\partial n}{\partial t} + \frac{\partial (Gn)}{\partial L} + n\frac{Q}{V} + D(L) - B(L) = 0, \tag{9}$$

where *G* is the growth rate, and *n* is the number of particles; *Q*, *D*, and *B* are the nucleation rates, and *L* is the arithmetic mean of the particle diameter. Further details on all the simplifications required to obtain the general population balance equation can be obtained from [34-36].

$$n = n^{\mathrm{o}}\exp\left[\frac{-L}{G\tau}\right], \tag{10}$$

where n^{o} is the density of the initial nucleus population and τ is the average residence time of the suspension, linearizing the **Eq.** (10), one obtains:

$$\ln n = \ln n^{o} - L\left(\frac{1}{G\tau}\right). \quad (11)$$

The log of population density (ln*n*) should vary linearly with the particle size (*L*). The kinetic parameters, $\ln n^{o} \mathrm{e} - 1/G\tau$, are determined from the linear and angular coefficients. The calculation is performed by disregarding the endpoints of the line. The average residence time, is calculated using **Eq.** (12).

$$\tau = \frac{V_{mixing}}{F_S + F_{CO_2}}, \quad (12)$$

where V_{mixing} is the volume of the organic mixture (solute and organic solvent), F_S is the flow rate of the solution, and F_{CO_2} is the volumetric flow rate of carbon dioxide, calculated from the density (ρ_{CO_2}) of carbon dioxide at the temperature and pressure of the system. By definition, the nucleation rate, B^{o}, is calculated using **Eq.** (13).

$$B^{o} = n^{o}G. \quad (13)$$

The experimentally obtained particle size distribution should be converted to population density *n* (*L*) before proceeding with the analysis of precipitation kinetics. The population density in each size range can be determined by **Eq.** (14).

$$n_L = \frac{M_T \Delta W}{k_V \rho_c L^3 \Delta L}, \quad (14)$$

where ρ_c is the particle density and *L* varies between L_1 and L_2. $\Delta L = L_2 - L_1$ is the width of the range size, and k_v is the volumetric shape factor for a sphere with a diameter equal to π/6. Δ*W* is the mass fraction of the particle size range L_1-L_2. The individual mass of each particle, *W*, is calculated using **Eq.** (15) considering that the particles are spherical with diameter *d*.

$$W = \frac{\pi d^3 \rho_c}{6}. \quad (15)$$

The density of the suspension, M_T, is calculated using **Eq.** (16).

$$M_T = \left(\frac{F_S}{F_S + F_{CO_2}(T)}\right) C, \quad (16)$$

where *C* [kg.m^{-3}] is the solute concentration in the feed solution.

3. Methodology

In the SAS process studied, solute and the organic solvent mixture enter the chamber center through a capillary tube with a micrometric diameter. The anti-solvent supercritical fluid enters laterally, provoking a turbulent jet that accelerates the mixing process and triggers rapid mass transference between the solution and the anti-solvent. The precipitation chamber of the SAS apparatus modeled in this study is schematically presented in Figure 1. The precipitation chamber

has a volume of 210 ml. The supercritical fluid (CO_2) inlet has a diameter of 2.5 mm, and it's located on the lid of the chamber, close to the lateral wall. The solution is fed through a capillary tube of a diameter of 0.125 mm positioned in the center of the chamber. The dimensions were obtained from the work of [25], which used ethanol as an organic solvent at a temperature and pressure of 313 K and 130 bar, respectively. The same operational conditions of *T* and *p* were employed in this work.

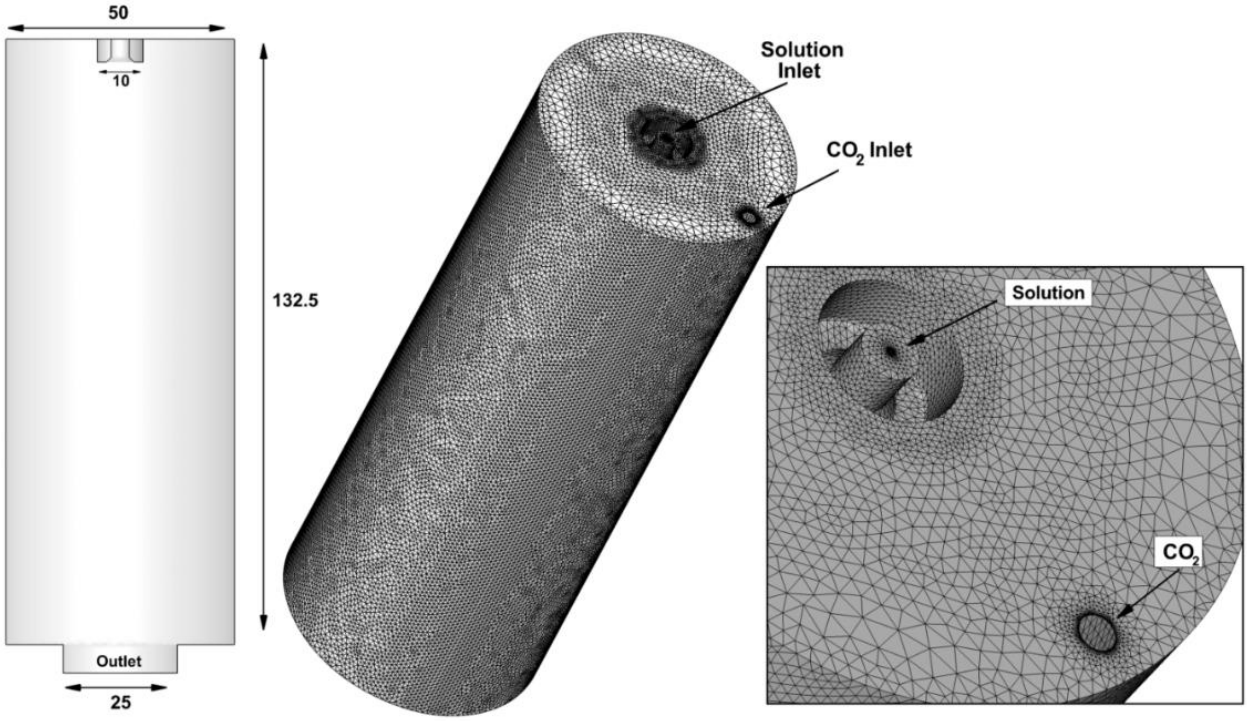

Figure 1 Dimensions and mesh of the precipitation chamber. Image zoom in the region of the CO_2 and solution inlets.

The chamber's geometry generated a sequence of three three-dimensional meshes with tetrahedral elements using the software Ansys Icem 14.5. After preliminary simulation studies, it was observed that the region of jet development is influenced by the mesh resolution (coarser meshes give more scattered jets with more considerable lengths). Therefore, specific refinements near the chamber walls and in the region of the CO_2 and ethanol jets formed were made to test the dependence of the solution with the mesh resolution (density of mesh elements). The third mesh (1.2×10^6 elements) resulted in a jet velocity that practically did not change about the second mesh considered. Thus, for the simulations of this work, the mesh composed of 1.2×10^6 elements was chosen, since more considerable refining did not bring any changes in the velocity field nor the shape of the jet.

Mass flow rate boundary conditions for ethanol and CO_2 inlets are shown in Table 1 for turbulence intensity conditions of 1%. Pressure condition was imposed at the outlet of the chamber.

Table 1 CO_2 and ethanol inlet flow rates used as simulation boundary conditions. Comparison of CFD results with experimental data reported in the literature.

	CO_2 Flow rate [l/min]	**Ethanol Flow rate [ml/min]**	**V_{CO_2} [m/s] (Inlet)**	**$V_{Ethanol}$ [m/s] (Inlet)**	**C_0 [mg/ml]**	**Experimental MPD [nn]**	**CFD MPD [nm]**	**Error %**
Case 1	6.56	0.3	22.27	4.07	10.0	-	223.36	-
Case 2	6.56	1.0	22.27	13.58	10.0	-	250.72	-
Case 3	6.56	2.0	22.27	27.16	10.0	-	242.15	-
Case 4	3.28	0.3	11.14	4.07	10.0	-	154.86	-
Case 5	3.28	1.0	11.14	13.58	10.0	-	134.9	-
Case 6	3.28	2.0	11.14	27.20	10.0	-	206.1	-
Case 7	6.56	1.0	22.27	13.58	1.0	277.0	250.7	9.5
Case 8	6.56	1.0	22.27	13.58	5.0	293.0	270.4	7.7
Case 9	6.56	0.3	22.27	4.07	10.0	176.0	196.2	-11.4

Subroutines for the density and viscosity of the mixture shown in **Eq.** (1) and (4), respectively, were implemented in C language and interpreted in Ansys Fluent software. Pressure-velocity coupling was used as the solution method Coupled algorithm for pseudo-transient flow with a pseudo-time step of 0.001 s, and first-order spatial discretization was employed. The system achieved average convergence of 5,000 interactions with residues in the order of 10^{-3} for the mass conservation and 10^{-5} for the other equations. The system showed a good convergence rate when the following steps were applied. First, turbulence convergence, movement quantity, and continuity equations were achieved; Second, equations of species transports were activated. Once these fields converge, the balance equation starts to be edited, followed by nucleation rate equations. A computer with an Intel (R) Core (TM) i7-7700HQ CPU @2. 8 GHz, (RAM) memory of 16 Gb with Windows 10, 64 bits operating system was used. The computing tie was, on average, 72 hours in each case.

4. Results and Discussion

4.1 Validation Test of the CFD Model

An experimental case reported by [25] in the literature validates the presented model. The experiments were conducted at pressure and temperature of 13 MPa and 313 K, respectively, and a CO_2 flow rate of 6.56 l/min. Ethanol flow rates and solid concentrations are shown in Table 1.

The results obtained by CFD simulations show the same trend as those obtained experimentally (Figure 2) with a mean error of 9.5%. An increase in the initial concentration of solids from 1.0 mg/ml to 5.0 mg/ml led to an increase of 12 nm in the MPD, both in the experiment and the simulation. On the other hand, at higher concentrations (10.0 mg/ml) of solute, the MPD decreases because the drop was smaller in the numerical experiment. The observed behavior is also corroborated by the numerical experimental work of [7], even if the particle size model proposed in this paper is more straightforward than those presented by [7, 21], and these authors observed a mean error of ±9.53% in MPD.

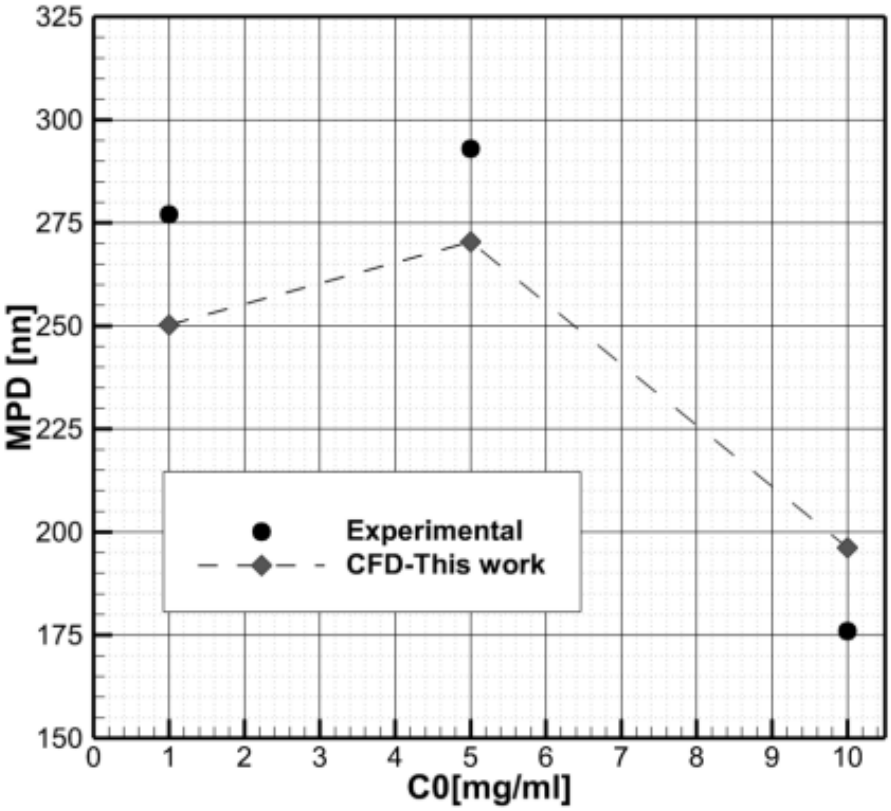

Figure 2 Comparison of mean particle diameters in relation to the initial concentration of minocycline in solution: experimental data obtained by Cardoso et al. (2008) and by CFD simulation in this work.

4.2 Dynamics of Mixed Jet

The diameter of the CO_2 inlet is twenty times larger than the diameter of the solution (ethanol + solute) inlet. Thus, the ethanol jet is driven towards the CO_2 jet. A variation in CO_2 and ethanol flow rates changes the interaction between the jets and directly influences the behavior of the mixture (Figure 3 b and Figure 4 b). Consequently, the mass transfer, closely related to the mean particle size obtained at the end of the process, will be, affected [13, 24, 37].

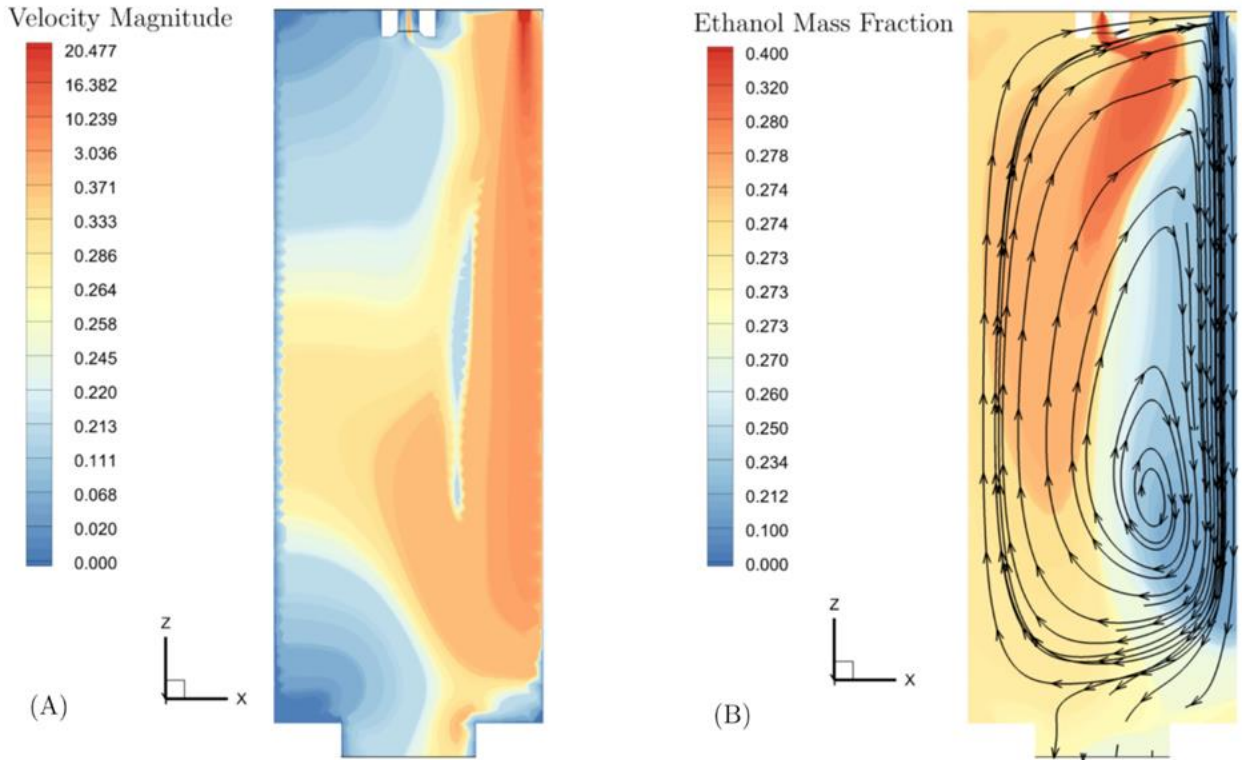

Figure 3 Velocity and ethanol mass concentration contours in a central cut plane of the chamber in case 1: (a) Velocity magnitude; (b) Ethanol mass fraction with 2D streamlines.

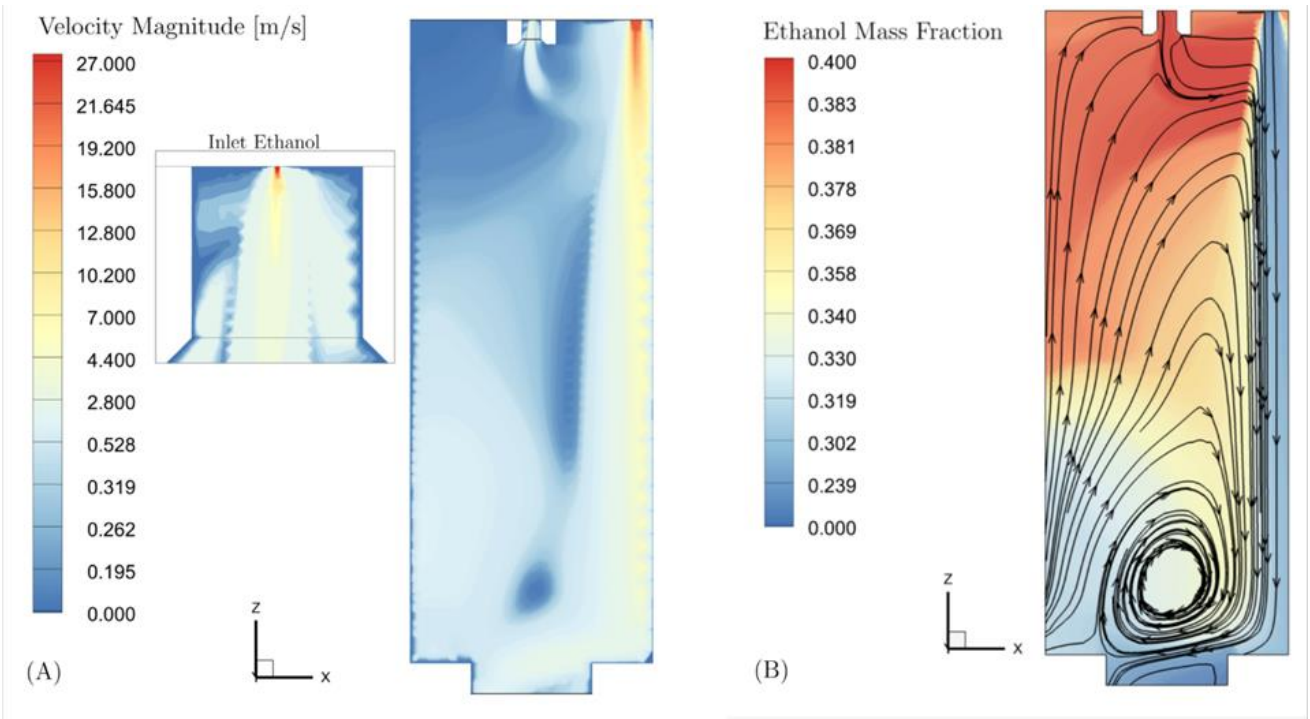

Figure 4 Velocity and ethanol mass concentration contours in a central cut plane of the chamber in case 3: (a) Velocity magnitude with the zoom at inlet ethanol region; (b) Ethanol mass fraction with 2D streamlines.

In case 1, the highest flow rate of CO_2 (6.56 l/min), generates high velocity around the carbon dioxide inlet, ~22.3 m/s. In contrast, the flow rate of ethanol is the lowest one considered (0.3 ml/min), which results in a velocity of approximately 4.1 m/s around the solution inlet and falls rapidly downstream. Therefore, the jet of solution loses momentum and is sucked by the plane of CO_2 already at the entrance region of the chamber, close to the lid, as shown in Figure 3 a b. The CO_2 inlet located on the lateral of the chamber generates an irregular contact zone between the solution jet and the carbon dioxide jet. The objective of the SAS process in the micronization process is to obtain suitable contact surfaces between the solvent and the antisolvent so that good mass transfer is possible [12]. The contact zone begins at the top of the chamber, where the CO_2 jet drags the jet of the solution going down to the bottom of the chamber at high velocity. Then, after hitting the bottom, the mixture recirculates again towards the top of the chamber, as shown in Figure 3 b by 2D streamlines. A richer mixture of ethanol is observed in the upper central region of the chamber (~4%), which decreases to approximately 2.7% at the bottom and the vicinity of the CO_2 inlet opposite wall.

In case 3, the CO_2 flow rate was kept constant at 6.56 l/min, and the highest ethanol flow rate (2.0 ml/min) was availed. A flow velocity of approximately 27.1 m/s was observed around the solution inlet. Similar to study case 1, the velocity decreases rapidly to around 5.3 m/s downstream due to the small diameter of the ethanol inlet shown in Figure 4 a.

In this case, just like in the previous case, the ethanol jet still deviates from the chamber's center towards the CO_2 jet, creating a contact zone further away from the center. Regular streamlines are generated downstream of the CO_2 inlet to the bottom of the chamber (Figure 4 b); close to this outlet region, a recirculation of fluids is observed, and a part of the mixture returns towards the top, and another part flows to the outlet. Compared to case 1, a greater ethanol-rich region is observed in case 3 in a larger chamber region. A vast region with a 4.0% mass fraction of ethanol is kept in the upper half part of the chamber (Figure 4 b). The mass fraction of ethanol decreases to approximately 3.4% in the middle of the chamber, and an average of 0.12% of ethanol is observed at the bottom near the exit.

An increase in the flow rate of the solution and, therefore, an increase in the velocity of the ethanol jet (Figure 4 a) makes contact of the anti-solvent with the ethanol difficult; That is, less anti-solvent makes contact with the solution, mass transference is slow, and supersaturation is low, which leads to a low nucleation rate and a higher particle growth [18, 19].

Calculated MPD, CO_2/ethanol flow rates, and inlet jet velocities are reported in Table 1 for each study case. Due to the higher CO_2 flow rate (6.56 l/min) and increased solution velocity at the chamber's inlet, an increase in MPD was observed in case 1 about case 2. A further increase in the velocity of the solution jet at the inlet of the chamber results in a decrease in MPD observed in case 2 compared to case 3. This may be because higher flow rates of the solution may also favor a better mixing inside the chamber, generating high rates of supersaturation, which results in smaller particles.

On the other hand, at the lowest CO_2 flow rate (3.28 l/min) evaluated and increasing the jet velocity of the solution at the inlet of the chamber, a decrease in the MPD was observed in cases 4 and 5. According to Table 1, a further increase in the velocity of the solution inside the chamber resulted in an increase in the MPD for case 5 and case 6. The relation of the MPD with the rise in the solution flow is also observed in the experimental work of [25]. Thus, in these conditions, the

interaction between the solution and anti-solvent jets is a complex and essential factor that directly affects the size of the particles obtained by the SAS process.

Three-dimensional streamlines, shown in Figure 5, reveal the flow patterns due to the chamber geometry and variations in the flow rates of CO_2 and ethanol for case 3. The mixing process inside the supercritical anti-solvent chamber involves diffusive and convective transport, turbulent diffusion, and multiple time scales related to fluctuations in concentration and velocity. The high velocity of the CO_2 jet with the ethanol flow rate of 2.0 ml/min makes the ethanol-rich CO_2 jet hit the bottom of the chamber where an intense mixing zone is formed.

Figure 5 Influence of CO_2 flow rate variations on flow streamlines at a constant flow rate of ethanol.

A large recirculation zone of the mixture was observed near the center and closer to the bottom of the chamber; part of this mixture rises again towards the CO_2 and ethanol inlets (another part heads towards the outlet) might think that nucleation is favored over molecular growth. The trend is to be formed smaller particle sizes in the order of $2.0e^{-7}$ [m], as seen in the following sessions.

4.3 CO_2 Flow Rate Influence

Particle size is a critical parameter for prolonged drug release processes. Reducing the particle size of bioactive compounds leads to an increase in the dissolution rate of the drug in the organism. Consequently, it increases its bioavailability, reduces the dose of medicine ingested, reduces the side effects, and minimizes the costs. The flow rates interfere with the jet-breaking regime and nucleation kinetics [38]. For example, in experimental literature work, with even higher CO_2 flow rates, 20-130 l/ml, at p = 120 bar and T = 313 K, c_0 = 5 g/l and constant flow rate of the solution of 1.5 ml/min, the size of particles precipitated in the SAS process decreases with increasing CO_2 flow rate. The reduction was observed because the quantity of CO_2 fed into the system is higher as its velocity inside the chamber. This process results in faster mass transference between the solution jet and the anti-solvent favoring solvent extraction and promoting higher nucleation rates, which leads to the formation of small uniform particles [19].

The variation of solvent and anti-solvent flow rate is essential for precipitation. Combining these two process variables can produce many types of morphologies and different sizes of particles [17, 38]. The CO_2 flow rates evaluated in the present work are much lower than those considered in the experimental work reported in the literature described above. Here, the observed trend was that: with the solute concentration of 10 mg/ml, an increase in CO_2 flow rate causes an increase in the average particle sizes at a constant flow rate of ethanol in all three situations studied, as shown in Figure 6, Figure 7 and Figure 8. The same behavior was reported by [37]: increasing the flow rate of CO_2 increases the mean particle size for similar conditions to those employed in this numerical work. According to this author, as the total flow is high, the amount of solute that remains dissolved in the fluid mixture leaving the precipitation chamber is high, causing a decrease in the maximum supersaturation and increasing the average particle size.

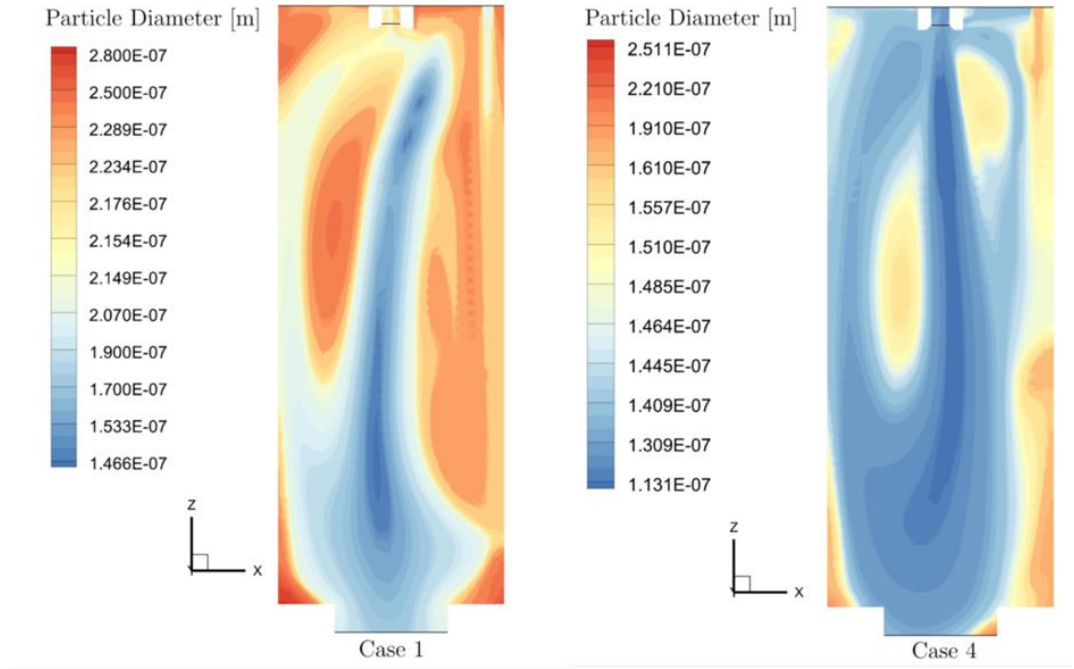

Figure 6 Particle diameter contours in a central section plane of the chamber for an ethanol flow rate of 0.3 ml/min: CO_2 flow rate of 6.56 l/min (**case 1**) and CO_2 flow rate of 3.28 l/min (**case 4**), with $c_{0,}$ = 10 mg/ml.

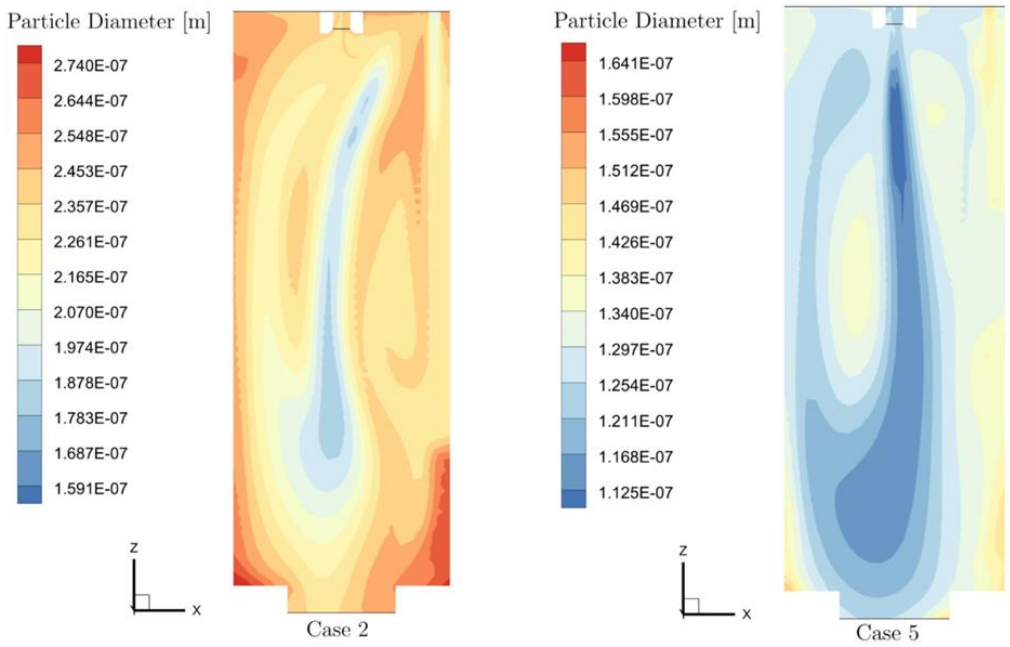

Figure 7 Particle diameter contours in a central section plane of the chamber for an ethanol flow rate of 1.0 ml/min and a CO_2 flow rate of 6.56 l/min (**case 2**), and a CO_2 flow rate of 3.28 l/min (**case 5**), with $c_{0,}$ = 10 mg/ml.

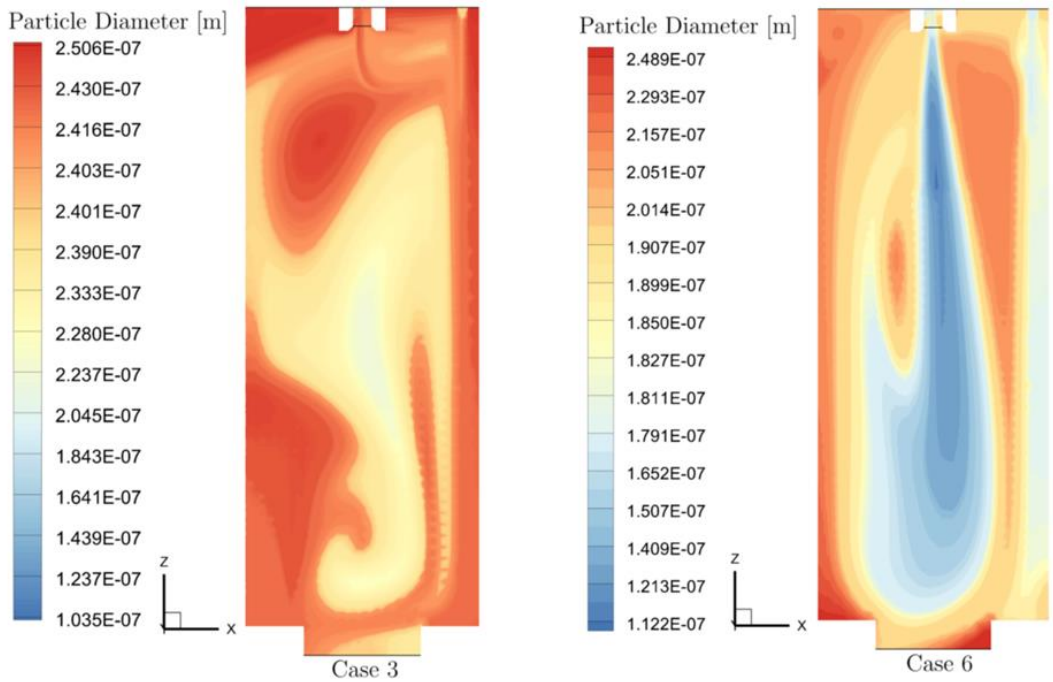

Figure 8 Particle diameter contours in a central section plane of the chamber for ethanol flow rate of 2.0 ml/min and: CO_2 flow rate of 6.56 l/min (**case 3**) and CO_2 flow rate of 3.28 l/min (**case 6**), with $c_{0,}$ = 10 mg/ml.

In all cases shown in the figures above, the smallest particle sizes are observed in the center of the chamber, where are also, ethanol-rich regions. For example, in case 3, which evaluates the largest ethanol flow rate studied, larger particle sizes are observed in Figure 8 compared to case 1, illustrated in Figure 6. So, the average particle diameter variable was plotted over the center line of

the chamber, which can be seen in Figure 9 and Figure 10. In the central line of the chamber, the variation of the mean particle diameters with the CO_2 flow rate for three different ethanol flow rates are shown in Figure 9; that is, an increase in the CO_2 flow rate led to a rise in the MPD for all cases of study. The highest MPD was observed in case 3, where the CO_2 flow rate was 6.56 l/min, and the ethanol flow rate was 2.0 ml/min. So, high flow rates can promote large particle sizes. Therefore, if the objective is to produce the smallest particle sizes under the conditions studied here, operating at the lowest CO_2 flow rate and moderate solution flow rates are necessary.

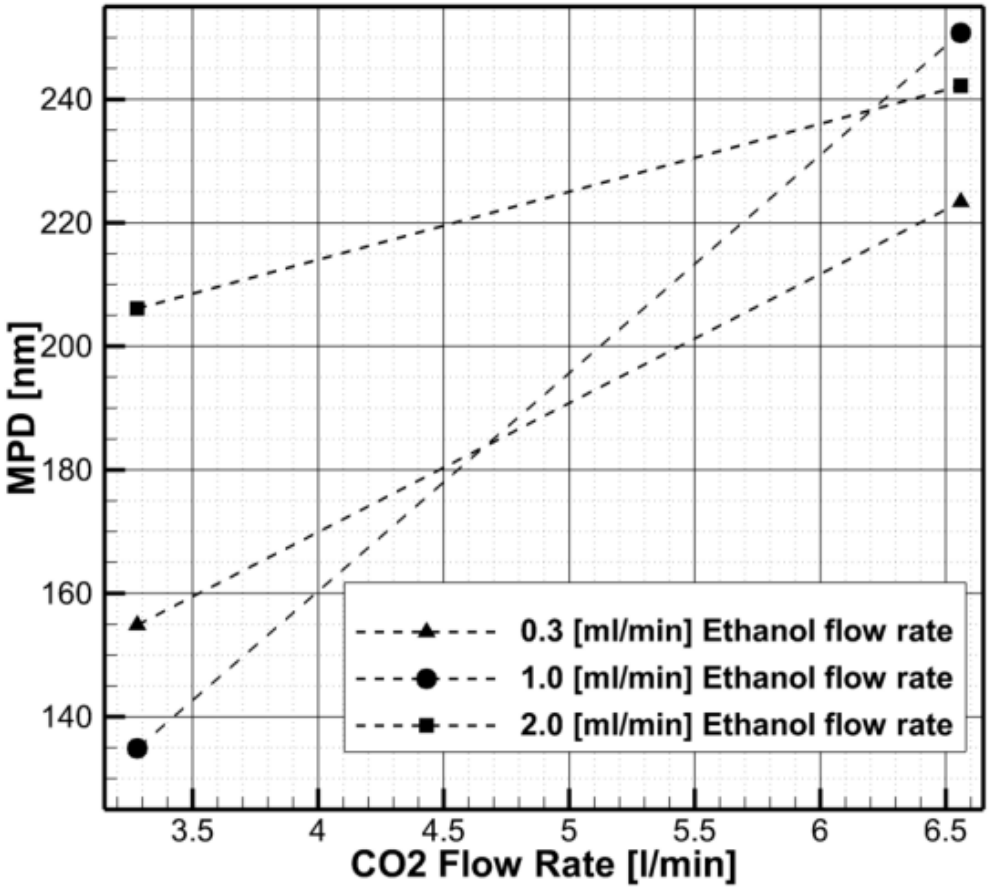

Figure 9 Variation of MPD with each CO_2 flow rate, for three different constant flow rates of ethanol (0.3 ml/min, 1.0 ml/min, and 2.0 ml/min).

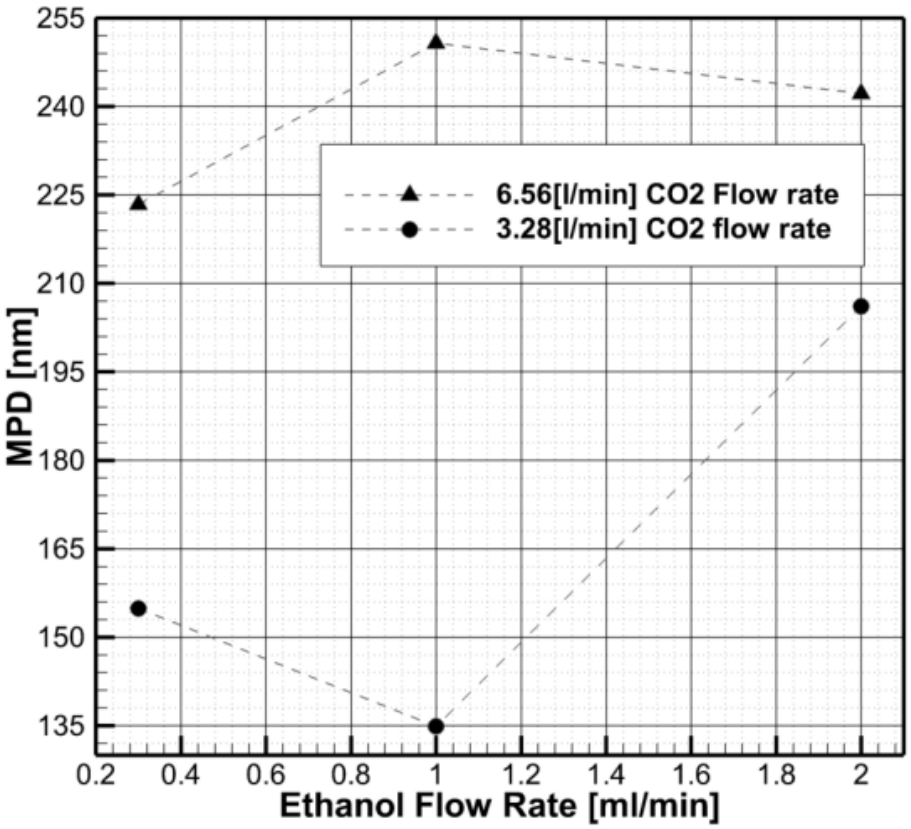

Figure 10 Variation of MPD with ethanol flow rate for two constant flow rates of CO_2 (6.56 l/ml and 3.28 l/ml).

4.4 Anti-Solvent Flow Rate Influence

At constant CO_2 flow rates of 6.56 l/min and 3.28 l/ml, the MPD inside the precipitation chamber was calculated individually, in the chamber center line, for each study case by varying the ethanol flow rate. The obtained results are shown in the graphic in Figure 10. At the highest CO_2 flow rate, it was observed that an increase in the flow rate of ethanol initially increases the MPD inside the precipitation chamber and then decreases. The initial behavior of the system can be explained by the collision between the solution jet at a low flow rate and, therefore, the low velocity at the inlet of the chamber and the supercritical CO_2 jet at a high flow rate, which is responsible for the breakage, disintegration into droplets and instantaneous atomization of the solution jet. Therefore, the energy per unit mass of liquid gained from supercritical CO_2 to disintegrate the solution into droplets decreases gradually, resulting in increased drop sizes and particle sizes.

However, as the solution flow rate increases, the energy per unit mass of liquid obtained from the dense gas for the solution breakdown into drops decreases. The fluid mixture and supercritical CO_2 interaction are weak enough for the liquid film to become wavy and disintegrate into drops. Under these conditions, the high velocity of the liquid solution produces tiny droplets and consequently smaller particle sizes, according to the theory of [39]. And [25] and [19] experimentally reported the same behavior for high CO_2 flow rates.

On the other hand, at the lowest CO_2 flow (3.28 l/min), the observed behavior of the MPD was different. Initially, a decrease in the MPD was observed. Then, a further increase in the flow rate of ethanol led to a rise in the MPD. The behavior of MPD under these conditions results from a

competition between the micro-mixing and nucleation, and growth kinetics. At a moderate flow rate of CO_2 (3.28 l/min), a slight increase in the solution flow rate from 0.3 ml/min to 1.0 ml/min resulted in a good mixture. A high rate of supersaturation and nucleation generated smaller particles, explaining the system's initial behavior and corroborating the reports [40].

A further increase in the solution flow rate from 1.0 ml/min to 2.0 ml/min increased the MPD, which was also reported by [18], according to whom increased solution flow rate, increases particle size. In this case, there is more solvent and less CO_2; therefore, mass transference is slower, probably resulting in low supersaturation. Also, it results in a lower nucleation rate, higher particle growth, and a widening of the particle size distribution due to differences in the growth rate of the formed crystals.

4.5 Temperature Variations

In the present model, the effects of temperature were considered in the particle precipitation process. Heat transport in the chamber can bring about important variations in particle sizes [27]. Considering the energy equation in the model's system of equations, **Eq**. (7) it is possible to measure local temperature variations inside the precipitation chamber. Local variations in temperature cause variations in density in the fluid, resulting in molecular homogeneities in the supercritical mixture, which can influence the particle size obtained [22, 41]. Figure 11 shows how the temperature variation occurs in the chamber, an effect of the mixture enthalpy. The inlet temperature was T = 313 K, the boundary condition at the inlets. Near the CO_2 and ethanol inlets, the mixture is cooling and reaching the bottom of the chamber on the opposite side of the CO_2 jet (isosurface at T = 305 K). On the other hand, the cooling near the CO_2 jet is less intense (isosurface at T = 310 K), and the temperature increases to 316 K at approximately 8 cm downstream of the CO_2 inlet. Through the central vertical sampling line of the chamber, there is a significant temperature variation (19.5 K) and also a significant variation in the particle diameters (~44 nm), as can be seen in the upper graph of Figure 11. In the bottom diagram of Figure 11 in the horizontal sampling line positioned at a distance Z = 0.06 [m] from the chamber lid, there is less variation in temperature (6.0 K) and also less variation in particle diameters (~16 nm). This pattern is generally observed after 4 cm downstream of the chamber lid: significant temperature variations are associated with large fluctuations in the particle diameters and vice versa.

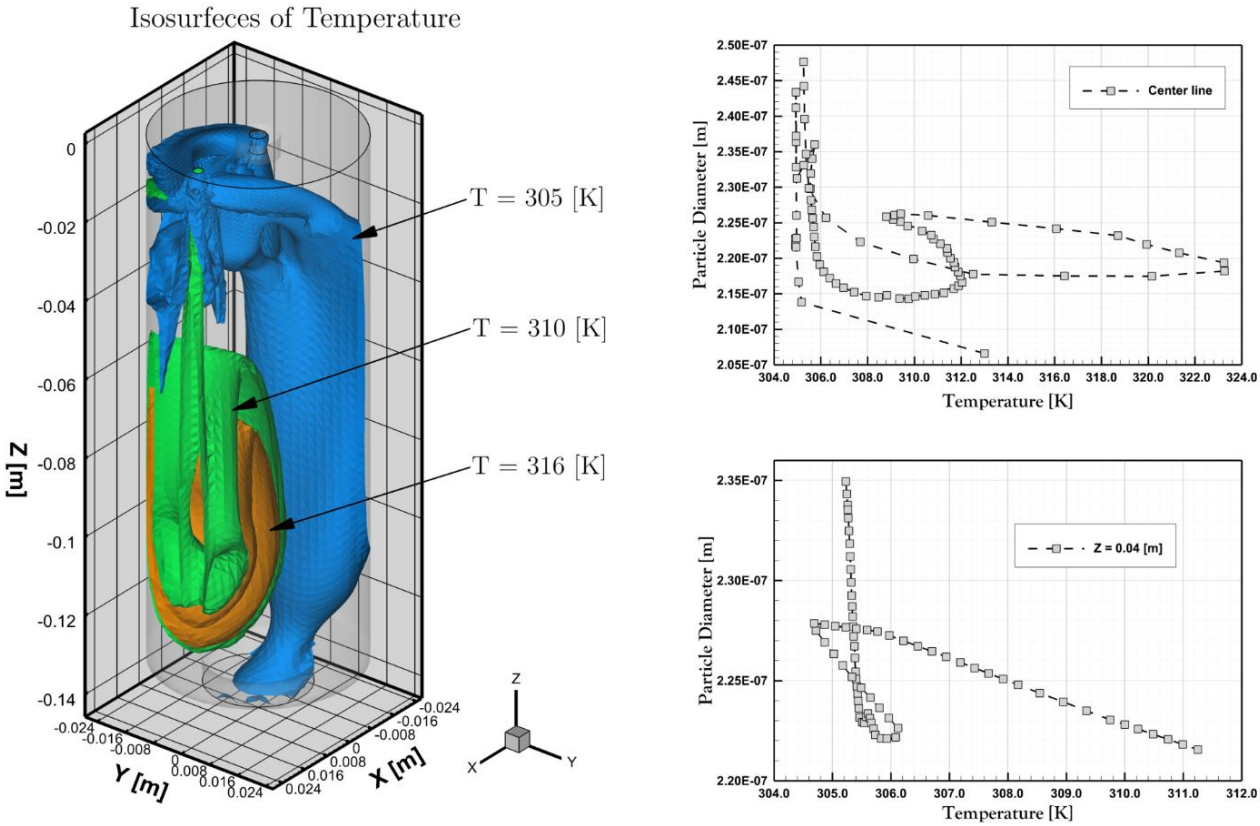

Figure 11 Isosurfaces of the temperature of three temperature values: T = 305 [K], T = 310 [K], and T = 316 [K]; plots of particle diameters versus temperature for vertical center line and horizontal line in Z = 0.04 m in **case 1**.

5. Conclusions

A mathematical model in a non-isothermal regime with the mass transfer was proposed to describe the dependence of particle sizes with high CO_2 flow rates on the precipitation of minocycline using the SAS process; it was numerically solved since there are still few numerical works in this sense.

This study contributes to a better understanding of the dynamics of particle precipitation; since there are few numerical works in the literature focusing on the flow rate variation, as well as employing a non-isothermal approach, the presented model requires little CPU time, proving to be an effective tool for understanding the influence of process parameters on the SAS technique.

Different ethanol and CO_2 flow rates were evaluated. The obtained results fit well with the experimental data described in the literature. Thus, from the proposed methodology, it will be possible to adjust the flow rates to appropriate values for when the objective is to increase or decrease particle sizes on a nanometric scale; it was also possible to obtain the temperature variation in the chamber and the dependence between particle sizes and temperature.

At higher CO_2 flow rates, an increase in the ethanol flow rate is followed by a rise in the mean particle diameter. Therefore, if the objective is to obtain small mean diameters, it is indicated to maintain a moderate flow rate of CO_2 and ethanol; in this process conditions, the smallest MPD was obtained.

Since the temperature variation was considerable, ~11 K, in future work, the phenomenon of particle agglomeration should be added to the current model. In this sense, the next step for this work will be comparing a wide range of experimental operational conditions. In particular, how chamber geometry and lengths/diameters of injection capillary tubes affect the precipitation mechanisms will be investigated.

Acknowledgments

The authors would like to thank: CNPQ (Grant No. 304804/2015-0) and CAPES (Grant No. 3006/2014).

Author Contributions

Dr Almeida, Dr. Rezende, Dr. Heitz Cardoso and Dr. Cardozo-Filho was responsible for model formulation and adequacy of input data. Dr. Almeida and Dr. Rezende were responsible for generating the meshes, adapting the numerical schemes for the convergence of the studied cases and interpretation of the results. Dr. Almeida was responsible for writing and final revising the article. Dr. Cardozo Filho leads research on precipitation of nanoparticles with supercritical CO_2 at the Laboratory of Supercritical Technology and Phase Equilibrium - LTSEF, without which it would be impossible to obtain the results of this article.

Competing Interests

On behalf of all authors, the corresponding author states that there is no conflict of interest.

References

1. Abadian M, Sodeifian G, Razmimanesh F, Mahmoudabadi SZ. Experimental measurement and thermodynamic modeling of solubility of Riluzole drug (neuroprotective agent) in supercritical carbon dioxide. Fluid Phase Equilib. 2023; 567: 113711.
2. Sodeifian G, Sajadian SA, Ardestani NS. Experimental optimization and mathematical modeling of the supercritical fluid extraction of essential oil from Eryngium billardieri: Application of simulated annealing (SA) algorithm. J Supercrit Fluids. 2017; 127: 146-157.
3. Sodeifian G, Sajadian SA, Derakhsheshpour R. CO_2 utilization as a supercritical solvent and supercritical antisolvent in production of sertraline hydrochloride nanoparticles. J CO_2 Util. 2022; 55: 101799.
4. Cardoso FAR, Rezende RVP, Almeida RA, Mezzomo N, Ferreira SRS, Meier HF, et al. CFD-based modeling of precipitation by supercritical anti-solvent process of microparticles from grape pomace extract with population balance approach. J Supercrit Fluids. 2018; 133: 519-527.
5. Jaouhari T, Marre S, Tassaing T, Fery-Forgues S, Aymonier C, Erriguible A. Investigating nucleation and growth phenomena in microfluidic supercritical antisolvent process by coupling in situ fluorescence spectroscopy and direct numerical simulation. Chem Eng Sci. 2022; 248: 117240.
6. Cardoso FAR, Almeida RA, Rezende RVP, Meier HF, Noriler D, Guerra HP, et al. Evaluation of changes in physicochemical properties in a supercritical antisolvent (SAS) process using 3D turbulent CFD approach. J Supercrit Fluids. 2016; 107: 349-357.

7. Henczka M, Bałdyga J, Shekunov BY. Particle formation by turbulent mixing with supercritical antisolvent. Chem Eng Sci. 2005; 60: 2193-2201.
8. Martín A, Cocero MJ. Numerical modeling of jet hydrodynamics, mass transfer, and crystallization kinetics in the supercritical antisolvent (SAS) process. J Supercrit Fluids. 2004; 32: 203-219.
9. Sodeifian G, Razmimanesh F, Sajadian AS. Solubility measurement of a chemotherapeutic agent (imatinib mesylate) in supercritical carbon dioxide: Assessment of new empirical model. J Supercrit Fluids. 2019; 146: 89-99.
10. Sodeifian G, Sajadian SA, Ardestani NS. Optimization of essential oil extraction from Launaea acanthodes Boiss: Utilization of supercritical carbon dioxide and cosolvent. J Supercrit Fluids. 2016; 116: 46-56.
11. Razmimanesh F, Sodeifian G, Sajadian AS. An investigation into Sunitinib malate nanoparticle production by US-RESOLV method: Effect of type of polymer on dissolution rate and particle size distribution. J Supercrit Fluids. 2021; 170: 105163.
12. Lestari SD, Machmudah S, Winardi S, Nurtono T, Wahyudiono, Kanda H, et al. Effect of solvent selection and nozzle geometry on curcuma mangga micronization process using supercritical antisolvent: Experiment and CFD simulation. Food Bioprod Process. 2020; 123: 367-377.
13. Obrzut DL, Bell PW, Roberts CB, Duke SR. Effect of process conditions on the spray characteristics of a PLA + methylene chloride solution in the supercritical antisolvent precipitation process. J Supercrit Fluids. 2007; 42: 299-309.
14. Daneshyan S, Sodeifian G. Synthesis of cyclic polystyrene in supercritical carbon dioxide green solvent. J Supercrit Fluids. 2022; 188: 105679.
15. Reverchon E, Adami R, Caputo G, De Marco I. Spherical microparticles production by supercritical antisolvent precipitation: Interpretation of results. J Supercrit Fluids. 2008; 47: 70-84.
16. Sodeifian G, Sajadian AS. Utilization of ultrasonic-assisted RESOLV (US-RESOLV) with polymeric stabilizers for production of amiodarone hydrochloride nanoparticles: Optimization of the process parameters. Chem Eng Res Des. 2019; 142: 268-284.
17. Bristow S, Shekunov T, Shekunov BY, York P. Analysis of the supersaturation and precipitation process with supercritical CO_2. J Supercrit Fluids. 2001; 21: 257-271.
18. Franceschi E, Kunita MH, Tres M V, Rubira AF, Muniz EC, Corazza ML, et al. Phase behavior and process parameters effects on the characteristics of precipitated theophylline using carbon dioxide as antisolvent. J Supercrit Fluids. 2008; 44: 8-20.
19. He WZ, Suo QL, Jiang ZH, Shan A, Hong HL. Precipitation of ephedrine by SEDS process using a specially designed prefilming atomizer. J Supercrit Fluids. 2004; 31: 101-110.
20. Neurohr C, Erriguible A, Laugier S, Subra-Paternault P. Challenge of the supercritical antisolvent technique SAS to prepare cocrystal-pure powders of naproxen-nicotinamide. Chem Eng J. 2016; 303: 238-251.
21. Sierra-Pallares J, Marchisio DL, Parra-Santos MT, García-Serna J, Castro F, Cocero MJ. A computational fluid dynamics study of supercritical antisolvent precipitation: Mixing effects on particle size. AIChE J. 2012; 58: 385-398.
22. Bałdyga J, Kubicki D, Shekunov BY, Smith KB. Mixing effects on particle formation in supercritical fluids. Chem Eng Res Des. 2010; 88: 1131-1141.
23. Zhang F, Marre S, Erriguible A. Mixing intensification under turbulent conditions in a high

pressure microreactor. Chem Eng J. 2020; 382: 122859.
24. Mukhopadhyay M, Dalvi SV. Mass and heat transfer analysis of SAS: Effects of thermodynamic states and flow rates on droplet size. J Supercrit Fluids. 2004; 30: 333-348.
25. Cardoso MT, Cabral JM, Palavra AM, Geraldes V. CFD analysis of supercritical antisolvent (SAS) micronization of minocycline hydrochloride. J Supercrit Fluids. 2008; 47: 247-258.
26. Bałdyga J, Makowski Ł, Orciuch W. Interaction between mixing, chemical reactions, and precipitation. Ind Eng Chem Res. 2005; 44: 5342-5352.
27. Cabeza LF, de Gracia A, Fernández AI, Farid MM. Supercritical CO_2 as heat transfer fluid: A review. Appl Therm Eng. 2017; 125: 799-810.
28. Imsanguan P, Pongamphai S, Douglas S, Teppaitoon W, Douglas PL. Supercritical antisolvent precipitation of andrographolide from andrographis paniculata extracts: Effect of pressure, temperature and CO_2 flow rate. Powder Technol. 2010; 200: 246-253.
29. Badens E, Boutin O, Charbit G. Laminar jet dispersion and jet atomization in pressurized carbon dioxide. J Supercrit Fluids. 2005; 36: 81-90.
30. Erriguible A, Fadli T, Subra-Paternault P. A complete 3D simulation of a crystallization process induced by supercritical CO_2 to predict particle size. Comput Chem Eng. 2013; 52: 1-9.
31. Cardoso FAR, Rezende RVP, Almeida RA, Cabral VF, Zanoelo EF, Noriler D, et al. A model for precipitation of sub-micrometric particles of PHBV poly (3-hydroxybutyrate-co-3-hydroxyvalerate) by supercritical assisted-atomization. J Supercrit Fluids. 2015; 97: 88-99.
32. Thakur AK, Kumar R, Kumar VV, Kumar A, Gaurav GK, Gupta KN. A critical review on thermodynamic and hydrodynamic modeling and simulation of liquid antisolvent crystallization of pharmaceutical compounds. J Mol Liq. 2022; 362: 119663.
33. Randolph AD, Larson MA. Theory of particulate processes: Analysis and techniques of continuous crystallization. 2nd ed. London: Academic Press; 1988. p. 386.
34. Boutin O. Modeling of griseofulvin recrystallization conducted in a supercritical antisolvent process. Cryst Growth Des. 2009; 9: 4438-4444.
35. Chiu HY, Lee MJ, Lin HM. Vapor-liquid phase boundaries of binary mixtures of carbon dioxide with ethanol and acetone. J Chem Eng Data. 2008; 53: 2393-2402.
36. Wu CS, He SL, Zhu DX, Gu M. Numerical simulation of microbubble flow around an axisymmetric body. J Hydrodynam. 2006; 18: 215-220.
37. Franceschi E. Precipitação e encapsulamento de beta-caroteno em PHBV empregando tecnologia supercrítica. Doctoral thesis. Graduate Program in Engineering Foods. Federal University of Santa Catarina - UFSC. 2009.
38. Bevilaqua Rosa G. Produção de micro e nanopartículas utilizando fluidos supercríticos. 2015.
39. Lefebvre AH. Energy considerations in twin-fluid atomization. J Eng Gas Turbines Power Jan. 1992; 114: 89-96.
40. Duarte ARC, Gordillo MD, Cardoso MM, Simplício AL, Duarte CMM. Preparation of ethyl cellulose/methyl cellulose blends by supercritical antisolvent precipitation. Int J Pharm. 2006; 311: 50-54.
41. Almeida RA, Rezende RVP, Cabral VF, Noriler D, Meier HF, Cardozo-Filho L, et al. The effect of system temperature and pressure on the fluid-dynamic behavior of the supercritical antisolvent micronization process: A numerical approach. Braz J Chem Eng. 2016; 33: 73-90.